Modeling Tritium Transport Through a Deep Unsaturated Zone in an Arid Environment

C. J. Mayers,* B. J. Andraski, C. A. Cooper, S. W. Wheatcraft, D. A. Stonestrom, and R. L. Michel

ABSTRACT

Understanding transport of tritium (^{3}H) in unsaturated zones is critical to evaluating options for waste isolation. Tritium typically is a large component of low-level radioactive waste (LLRW). Studies at the U.S. Geological Survey's Amargosa Desert Research Site (ADRS) in Nevada investigate ^{3}H transport from a closed LLRW facility. Two boreholes are 100 and 160 m from the nearest waste trench and extend to the water table at 110 m. Soil-water vapor samples from the deep boreholes show elevated levels of ^{3}H at all depths. The objectives of this study were to (i) test source thermal and gas-advection mechanisms driving ^{3}H transport and (ii) evaluate model sensitivity to these mechanisms and to selected physical and hydraulic properties including porosity, tortuosity, and anisotropy. A two-dimensional numerical model incorporated a non-isothermal, heterogeneous domain of the unsaturated zone and instantaneous isotopic equilibrium. The TOUGH2 code was used; however, it required modification to account for temperature dependence of both the Henry's law equilibrium constant and isotopic fractionation with respect to tritiated water. Increases in source temperature, pressure, and porosity enhanced ^{3}H migration, but failed to match measured ^{3}H distributions. All anisotropic simulations with a source pressure component resembled, in shape, the upper portion of the ^{3}H distribution of the nearest borehole. Isotopic equilibrium limited migration of ^{3}H, while effects of radioactive decay were negligible. A 500 Pa pressure increase above ambient pressure in conjunction with a high degree of anisotropy (1:100) was necessary for simulated ^{3}H transport to reach the nearest borehole.

UNDERSTANDING TRANSPORT of ^{3}H in unsaturated zones is critical for evaluating options for waste isolation and tracer study results. Smiles et al. (1995) explored the movement of ^{3}H in liquid and gas phases in a deep unsaturated zone using a spherically symmetric diffusion equation. Simulations predicted ^{3}H migrating <30 m in 100 yr. Because of numerical cancellation errors when applying the analytical solution of Carslaw and Jaeger (1959) to a nonpoint source, Smiles et al. (1995) used a point source to approximate initial conditions. Assuming transient effects of ^{3}H concentration do not persist, Knight (1996) derived a more accurate approximation for the initial conditions and found that the quantity of ^{3}H and its distribution dictated the final ^{3}H distribution. Neither of these studies evaluated the

effects of temperature dependence of the Henry's law equilibrium constant or isotopic fractionation with respect to ^{3}H.

Studies at the U. S. Geological Survey's ADRS in Nevada are investigating ^{3}H transport from a closed LLRW facility (Fig. 1). Striegl et al. (1996) attempted to explain elevated concentrations of tritiated water vapor (^{3}HHO$_g$) found throughout the unsaturated zone at a borehole 160 m from the nearest LLRW trench. They used diffusive (Smiles et al., 1995) and advective transport models to simulate an isothermal and homogeneous domain. The models were unable to match observed ^{3}HHO$_g$ concentrations. The diffusive model predicted ^{3}H migration to a maximum distance of approximately 10 m from the source after 30 yr. An order of magnitude increase in the effective diffusion coefficient increased the maximum distance by a factor of three. The advective model used a pressure originating from the source. Striegl et al. (1996) determined a 1300 Pa source-pressure-difference sustained for 30 yr was required to move the ^{3}H 100 m, but were unable to justify a source-pressure-difference >100 Pa. Ultimately, a conceptual model of lateral subsurface liquid transport from LLRW trenches was developed as a possible explanation for the observed high concentrations of ^{3}H in the unsaturated zone. However, Striegl et al. (1996) stated that it was not clear how this flow could have occurred and cited previous work at the site that showed no evidence of significant liquid water movement in the subsurface. Thus, the elevated ^{3}H concentrations in the deep and shallow unsaturated zone at the ADRS (Striegl et al., 1996; Healy et al., 1999) have caused speculation regarding the exact mechanisms that control ^{3}H transport in arid unsaturated zones.

This study combined field data and numerical modeling to further investigate ^{3}H transport in the deep unsaturated zone at the ADRS. The objectives were to (i) test source thermal and gas-advection mechanisms driving tritium transport and (ii) evaluate model sensitivity to these mechanisms and to selected physical and hydraulic properties including porosity, tortuosity, and anisotropy. Laboratory and field data allowed for conceptualization of flow processes, parameterization of the model, and evaluation of simulation results. The numerical model incorporated a non-isothermal, heterogeneous domain. The TOUGH2 code (Pruess et al., 1999) was used; however, it required modification to account for temperature dependence of both the Henry's law equilibrium constant and isotopic fractionation with respect to tritiated water.

C.J. Mayers and B.J. Andraski, U.S. Geological Survey, WRD, 333 West Nye Lane, Carson City, NV 89706. C.A. Cooper, Desert Research Institute, 2215 Raggio Parkway, Reno, NV 89512. S.W. Wheatcraft, Dep. of Geological Sciences, Univ. of Nevada, Reno, NV 89557. D.A. Stonestrom and R.L. Michel, U.S. Geological Survey, WRD, NRP, 345 Middlefield Road, Menlo Park, CA 94025. Received 17 Dec. 2004. *Corresponding author (cjmayers@usgs.gov).

Abbreviations: ADRS, Amargosa Desert Research Site; EOS, equation of state; ^{3}H, tritium; ^{3}HHO$_g$, tritiated water vapor; ^{3}HHO$_l$, tritiated liquid water; LLRW, low-level radioactive waste; MHE, maximum horizontal extent; MVE, maximum vertical extent; P$_S$, source-pressure difference above ambient; T$_S$, source temperature.
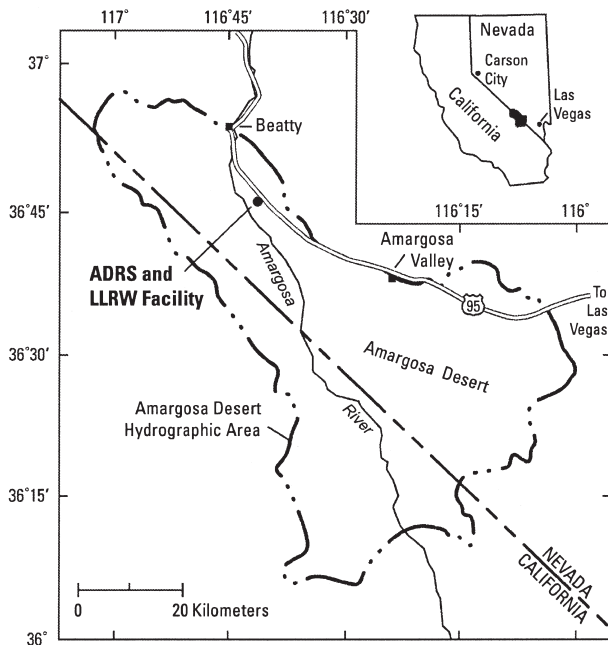
Fig. 1. Location map showing the Amargosa Desert Research Site (ADRS) and the low-level radioactive waste (LLRW) facility near Beatty, NV.

MATERIALS AND METHODS

Field Site and Data Collection

The field site is located 17 km south of Beatty and 169 km northwest of Las Vegas (Fig. 1). The unsaturated zone at the ADRS is approximately 110-m thick and comprises alluvial and fluvial deposits. Annual precipitation (1981–2002) averages 105 mm. The unsaturated zone at the ADRS has been drying for approximately 16 000 yr (Scanlon et al., 2003; Walvoord et al., 2004).

The LLRW facility buried waste from 1962 to 1992 in a series of 22 shallow trenches (Fig. 2). Trenches ranged from 2 to 15 m deep. Before burial, LLRW underwent dewatering or solidification. A 1976 U.S. Nuclear Regulatory Commission (USNRC) investigation, however, indicated that liquid wastes delivered to the LLRW facility between 1962 and 1975 were disposed of directly into the trenches (USNRC, 1976). Steps for burial of LLRW included excavating and stockpiling native sediments and emplacing waste and stockpiled sediments in layers. The LLRW trenches were not lined. During the operational life of the facility, trench covers were kept free of vegetation. Following closure of the LLRW facility a minimum of 2 m of stockpiled native sediments was used to cover all trenches.

Samples from three unsaturated-zone boreholes (UZB-1, UZB-2, and UZB-3) were analyzed for water content, bulk density, and particle-size; two boreholes (UZB-2 and UZB-3) were instrumented for collection of soil gas samples. Boreholes UZB-1 and UZB-2 are approximately 6-m apart and 160 m from the nearest LLRW trench (Prudic et al., 1997); UZB-3 is approximately 100 m from the nearest LLRW trench (Fig. 2). Boreholes UZB-1, UZB-2, and UZB-3 were drilled to depths of 48 m, 114.6 m, and 114.4 m in November 1992, September 1993, and December 1999, respectively. Water contents were measured by cryodistillation (Prudic et al., 1997). Particle-size distributions were determined by sieving and laser-light scattering (Gee and Or, 2002). Soil-water vapor sampling was based on methods discussed in Striegl (1988). The first soil-water vapor sampling at UZB-2 and UZB-3 began in April
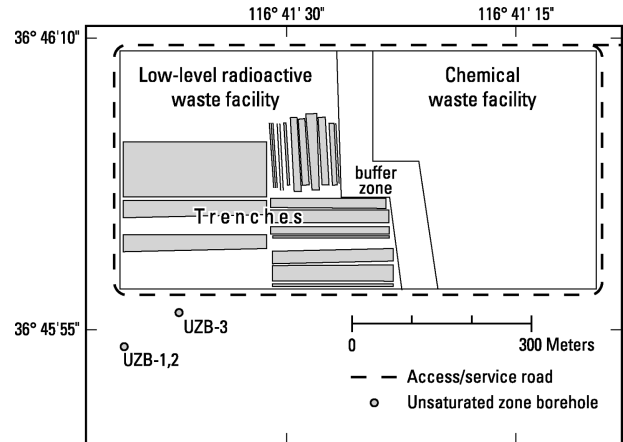

Fig. 2. Low-level radioactive waste facility, chemical waste facility, and deep unsaturated zone boreholes.

1994 and April 2000, respectively; subsequent sampling occurred annually. Tritium concentrations were measured by direct liquid-scintillation counting (Thatcher et al., 1977).

Numerical Model

The TOUGH2 code solves a nonlinear mass balance equation for all components included in the equation of state (EOS) module and an energy-balance equation for the system. The EOS7R module allows for the following components: water, brine, radionuclide 1 "parent," radionuclide 2 "daughter," and air. The van Genuchten-Mualem model (van Genuchten, 1980; Mualem, 1976) was used to calculate relative permeability and capillary pressure:

$$k_{rl} = \Theta^{1/2}[1 - (1 - \Theta^{1/m})^m]^2 \qquad [1]$$

$$P_{cap} = -\frac{\rho g}{\alpha}(\Theta^{-1/m} - 1)^{1-m} \qquad [2]$$

with

$$\Theta = \frac{(\theta - \theta_r)}{(\theta_s - \theta_r)} \qquad [3]$$

and

$$\theta = \theta_r + \frac{(\theta_s - \theta_r)}{[1 + |\psi\alpha|^n]^m} \qquad [4]$$

where k_{rl} is relative permeability as a function of water content; P_{cap} is capillary pressure; ρ is density of water; g is gravity; θ is volumetric water content; θ_r is residual water content; θ_s is saturated water content; ψ is pressure head; and α, n, and m are curve fitting parameters subject to $m = 1 - n^{-1}$ and $0 < m < 1$. The Corey (1954) gas relative permeability function used is

$$k_{rg} = (1 - \overline{\Theta})^2(1 - \overline{\Theta}^2) \qquad [5]$$

with

$$\overline{\Theta} = \frac{(\theta - \theta_r)}{(1 - \theta_r - \theta_{rg})} \qquad [6]$$

where k_{rg} is gas relative permeability, and θ_{rg} is residual gas content. The diffusive flux equation is

$$\mathbf{f}_\beta^\kappa = \phi\tau_0\tau_\beta\rho_\beta d_\beta^\kappa \nabla X_\beta^\kappa \qquad [7]$$

where $\mathbf{f}_\beta^\kappa$ is diffusive flux of component κ in phase β (liquid

or gas), ϕ is porosity, τ_0 is a porous medium dependent factor of tortuosity, τ_β is a tortuosity coefficient dependent on phase saturation, ρ_β is phase density, d_β^κ is diffusion coefficient of component κ in phase β, and X_β^κ is mass fraction of component κ in phase β. The Millington model (Millington, 1959) used to calculate the saturation-dependent tortuosity is

$$\tau_0\tau_\beta = \phi^{1/3}S_\beta^{10/3} \qquad [8]$$

where S_β is phase saturation. The temperature and pressure dependent diffusion coefficient (Vargaftik, 1975) is

$$d_\beta^\kappa(P,T) = d_\beta^\kappa(P_0,T_0)\frac{P_0}{P}\left(\frac{T + 273.15}{273.15}\right)^\vartheta \qquad [9]$$

where P is pressure, T is temperature, $P_0 = 101\,325$ Pa, $T_0 = 0°C$, and ϑ is the temperature dependence which is 1.8. Radioactive decay allows radionuclide 1 to decay into radionuclide 2.

$$\frac{d\mathbf{M}^\kappa}{dt} = -\lambda^\kappa\mathbf{M}^\kappa \qquad [10]$$

where $\mathbf{M}^\kappa$ is mass of radionuclide κ per unit volume, t is time, and λ^κ is the decay constant of radionuclide κ.

To more accurately test ^{3}H transport mechanisms, the TOUGH2 code was modified to include temperature effects on the gas and liquid partitioning of ^{3}H. A function was coded to account for temperature effects on both the Henry's law equilibrium constant and the isotopic fractionation factor for tritiated water:

$$HCRN1 = \frac{1}{k_{H-^3H}\alpha_{^3HHO}} \qquad [11]$$

with

$$k_{H-^3H} = \left[\frac{C_g}{C_{aq}}\right]R \qquad [12]$$

where $HCRN1$ is solubility constant of ^{3}HHO$_g$ in water, k_{H-^3H} is a temperature dependent Henry's law equilibrium constant for tritiated water, $\alpha_{^3HHO}$ is a temperature dependent fractionation factor for tritiated water, C_g is concentration of ^{3}H in water vapor, C_{aq} is concentration of ^{3}H in liquid water, and R is the ideal gas constant. Fractionation values for ^{3}H were obtained from Ferronsky and Polyakov (1982).

A single source trench was used to represent the 22 trenches at the LLRW facility (Fig. 3). The total volume of the LLRW trenches is approximately 7.35×10^5 m^3 and the greatest trench depth is 15 m below land surface. The three western-most trenches contain approximately 90% of ^{3}H disposed at the LLRW facility (Fig. 2) (Nevada State Health Division, unpublished data, 1992). The model simulated a representative 1-m wide vertical slice of the source trench along the A–A' transect. Projected onto the modeled slice for reference are the relative locations of the UZB-2 and UZB-3 boreholes (Fig. 3). A total ^{3}H radioactivity of approximately 1.27×10^{16} Bq (Nevada State Health Division, unpublished data, 1992) and an assumed backfill and LLRW water content of 0.05 m^3 m^{-3} resulted in a source-trench concentration of 3.46×10^8 Bq L^{-1}.

The model domain extended 585, 1, and 115 m in the x, y, and z directions, respectively (Fig. 4a). Due to the dimensions of the LLRW trenches and the close proximity of the area of interest to the trenches, the computational grid used Cartesian coordinates. The domain incorporated 2796 cells and the vertical grid spacing ranged from 1 to 4 m, while horizontal grid spacing ranged from 5 to 50 m. Cells close to the source trench and at lithologic contacts had a closer spacing.

Physical and hydraulic property data and other information defined a lithologic model of the site (Fig. 4b). Detailed data
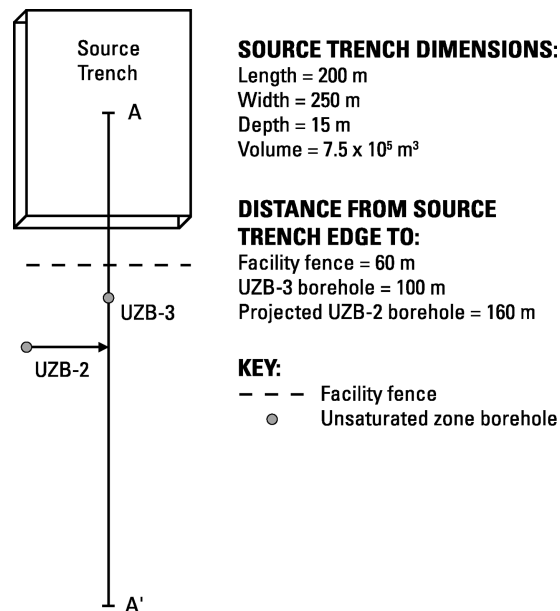
SOURCE TRENCH DIMENSIONS:
Length = 200 m
Width = 250 m
Depth = 15 m
Volume = 7.5 x 10⁵ m³

DISTANCE FROM SOURCE TRENCH EDGE TO:
Facility fence = 60 m
UZB-3 borehole = 100 m
Projected UZB-2 borehole = 160 m

KEY:
– – – Facility fence
● Unsaturated zone borehole

Fig. 3. Plan view of conceptualized source trench and 600-m transect, A–A'.

available for the upper 5 m of undisturbed sediments and for trench fill material (Andraski, 1996; Andraski and Jacobson, 2000) formed the basis for material properties assigned to the reference model (Table 1). Drillers' logs, gamma logs, particle-size distribution data, air permeability data, a profile description (Fischer, 1992), and photographs of a 20-m deep hazardous waste trench were used to define sediment layers below 5 m. Textural similarities formed the basis for assignment of properties of a sediment layer in the upper 5 m to a deeper sediment layer. Three distinct sediment types defined a layered model and included gravel, sandy gravel, and silty sand with gravel. The top of the water table was defined at 110 m below land surface.

Initial conditions for the reference model were generated using a steady-state simulation. The steady-state simulation used approximations for the two boundary conditions, land surface and 5 m below the water table (Table 2). Temperatures assigned at the land surface and 5 m below the water table were projected from mean daily thermocouple psychrometer data collected for 3 yr (2000–2002) between depths of 10.9 and 103.7 m. Gas-phase pressure at the land surface was based on a 3-yr mean daily of barometric pressure (1998–2000). Gas-phase pressure 5 m below the water table was a hydrostatic value (110 m of air and 5 m of water). Gas saturation at the land surface was based on average measured water potentials (-4 MPa) under native vegetation (Andraski, 1997) and the corresponding soil–water content that was calculated using the van Genuchten (1980) retention model. These boundary conditions resulted in steady-state temperature, pressure, and water content profiles shown in Fig. 5. The steady-state water content profile generated was, on whole, comparable in shape to the observed profile, but on average was 0.06 m^3 m^{-3} drier.

The transport simulation boundaries were: land surface, 5 m below the top of the water table, vertical boundary under the source trench (Fig. 4a, horizontal distance = 0 m), vertical boundary away from the source trench (Fig. 4a, horizontal distance = 585 m), and the horizontal and vertical faces of the source trench. All boundaries in the transport simulations had prescribed thermodynamic conditions except for the vertical axis of symmetry underneath the source trench, which was defined as a no flux boundary. In addition, the prescribed
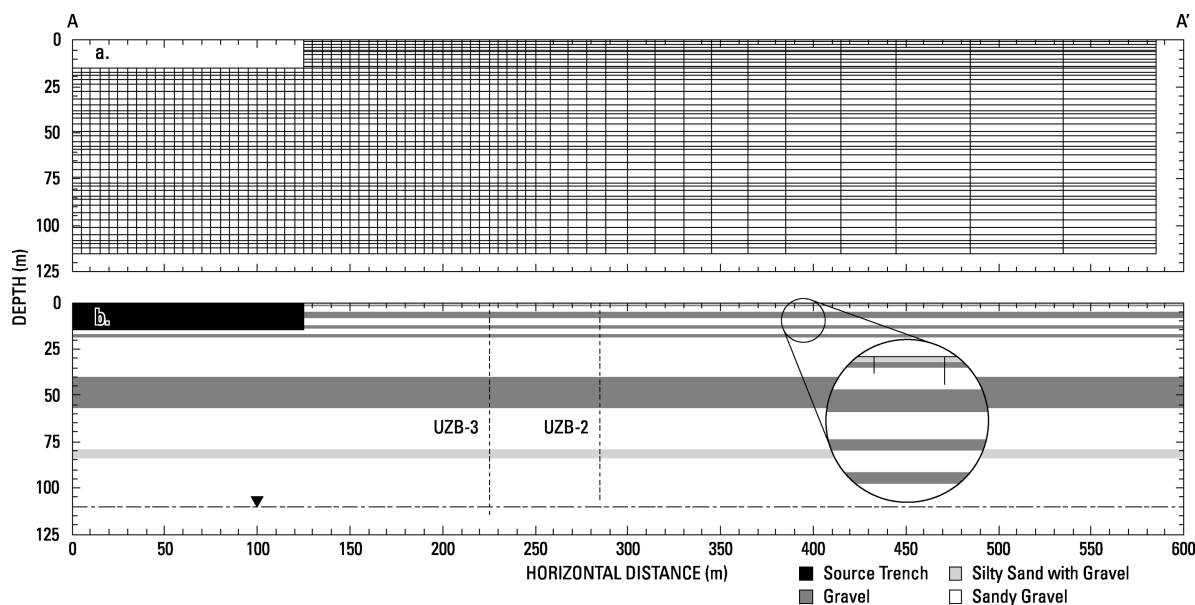
Fig. 4. (a) Computational grid and (b) lithology of modeled vertical slice along A–A' transect shown in Fig. 3. Locations of unsaturated zone boreholes UZB-2 and UZB-3 are included for reference (see Fig. 3).

boundaries along the faces of the source trench allowed the initial ^3H concentration to diminish by radioactive decay.

Overview of Model Assumptions and Numerical Simulations

All model simulations ran for 40 yr (1962–2002), which allowed comparison with field data collected from 1994 to 2002. Assumptions included instantaneous emplacement of LLRW at time = 0 yr and instantaneous isotopic equilibrium between the gas and liquid phases. The assumption of local equilibrium between aqueous and airborne species is consistent with theory given that in beaker-scale experiments, substantive equilibrium is attained on time scales of minutes (Logan, 1996). The rate-limiting step is diffusion in the liquid phase, and pore-scale liquid dimensions are small. Failure of the local equilibrium assumption would allow tritiated water vapor to move more quickly than theory predicts. Simulations used a maximum time step of 1 yr to avoid time discretization errors that occur when time steps approach the half-life of the simulated radionuclide. In addition to the reference model (described above), simulations were performed with variations in source temperature (T_S), source-pressure difference above ambient (P_S), material properties (porosity, tortuosity, anisotropic ratios of intrinsic permeability), and various combinations of T_S, P_S, and material properties (Table 3).

The similarities between LLRW facilities and municipal landfills formed the basis for increased temperatures and pressures in the source trench. The LLRW trenches are unlined and the final covers are monolithic; however, they contain

waste similar in type to waste buried at municipal landfills that is radioactive (Crawford and Smith, 1985; Fentiman et al., 1993). The temperatures and pressures within municipal landfills increase as a function of organic biodegradation. Lacking direct measurements from the LLRW facility, temperature, and pressure values were obtained from landfill literature. Temperatures within municipal landfills range from 25 to 45°C and gas pressures range from 250 to 500 Pa above atmospheric pressure (Crawford and Smith, 1985). The T_S values tested included 35 and 45°C. The P_S values tested were 100, 250, and 500 Pa. The source trench in the reference model had an average temperature of 22°C and average pressure of 9.18×10^4 Pa; temperatures and pressures based on initial conditions varied with depth. Striegl et al. (1996) did not consider biodegradation in the LLRW facility and estimated 100 Pa to be the maximum justifiable pressure difference at ADRS due to temperature and buoyancy effects. Combinations of T_S and P_S values also were tested and included simulations with a T_S of 45°C and P_S of 100, 250, and 500 Pa.

Model sensitivity to porosity was tested by setting material porosities to half the original porosity and twice the original porosity. The TOUGH2 code uses relative saturation for mass balance and flow processes, and the mass of the water present in the flow field was scaled appropriately for specified changes in porosity. In both cases, steady-state simulations were run to generate the associated initial conditions. Porosity-sensitivity testing included simulations run under reference model, T_S, P_S, and T_S and P_S conditions.

The saturation dependence of tortuosity is poorly under-

Table 1. Material properties of reference model.†

Parameter‡	Trench fill	Gravel	Sandy gravel	Silty sand w/gravel
Horizontal intrinsic permeability (m²)	2.96×10^{-13}	1.22×10^{-11}	3.77×10^{-12}	5.10×10^{-13}
Vertical intrinsic permeability (m²)	2.96×10^{-13}	1.22×10^{-11}	3.77×10^{-12}	5.10×10^{-13}
Porosity	0.252	0.182	0.240	0.322
Residual liquid saturation	0.001	0.001	0.001	0.001
α (Pa⁻¹)	5.12×10^{-4}	7.15×10^{-2}	4.36×10^{-3}	3.60×10^{-4}
m	0.190	0.155	0.134	0.227
Specific heat (J kg⁻¹ °C⁻¹)	967	864	930	790

† Based on Andraski (1996) and Andraski and Jacobson (2000).
‡ α and m are curve fitting parameters for the van Genuchten model.

Table 2. Model parameters and reference model boundary conditions.

Parameter	Value	
Diffusion coefficients (25°C)	Gas phase	Aqueous phase
Air (m² s⁻¹)	–	2.00×10^{-9}†
Water (m² s⁻¹)	2.60×10^{-5}†	–
Tritiated water (m² s⁻¹)	2.47×10^{-5}‡	2.24×10^{-9}§
Tritium half-life (yr)	12.35¶	
Boundary conditions		
Top (land surface)		
Gas pressure (Pa)	9.17×10^4	
Temperature (°C)	21.8	
Gas saturation	0.889	
Bottom (115-m depth)		
Gas pressure (Pa)	1.43×10^5	
Temperature (°C)	26.8	

† From Cussler (1997).
‡ Calculated on the basis of kinetic gas theory, using equation 23.3.8 of Atkins (1978).
§ From Mills (1973).
¶ From Evans (1974).

stood (Pruess et al., 1999). Given this uncertainty and a reference model simulation using the Millington (1959) tortuosity model, simulations also were run using a relation in which the saturation dependence of tortuosity is based on relative permeability (Pruess et al., 1999),

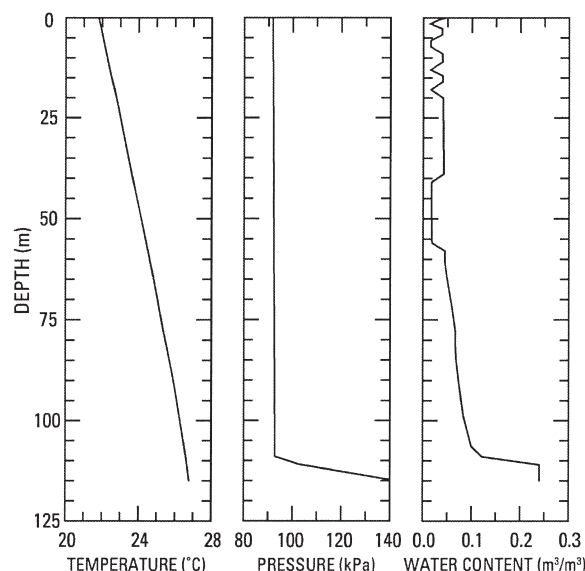$$\tau_0 \tau_\beta = \tau_0 k_{r\beta} \qquad [13]$$

where $k_{r\beta}$ is a saturation-dependent relative permeability in phase β and τ_0 is subject to the restriction $0 < \tau_0 \leq 1.0$. Model sensitivity to tortuosity was tested by setting tortuosity values to 0.66 and 0.99 for all materials. Tortuosity-sensitivity testing included simulations run under reference model, T_S, P_S, and T_S and P_S conditions.

Because of the nature of the alluvial and fluvial sediment deposition at the ADRS, it is likely that permeability is anisotropic with greater permeability along the horizontal plane. Saturated hydraulic conductivity and soil-water retention curves from repacked cores formed the basis for estimating the intrinsic permeability values of all materials (Andraski, 1996). The reference model had isotropic intrinsic permeability values for all materials. Model sensitivity to anisotropy was tested using two anisotropy ratios, 1:10 and 1:100. Freeze and Cherry (1979) state that it is not uncommon for layered heterogeneity to lead to regional anisotropy on the order of 1:100 or greater. Anisotropy-sensitivity included simulations run under reference model, T_S, P_S, and T_S and P_S conditions. The source-trench in all simulations remained an isotropic material, due to the homogeneity of the fill material after excavating and backfilling operations.

Fig. 5. Simulated steady state temperature, gas phase pressure, and water content profiles.

RESULTS AND DISCUSSION

Field Data

Volumetric water content ranged from 0.05 to 0.14 m³ m⁻³ (Fig. 6a). The average water content was 0.09 m³ m⁻³ above 40 m and 0.12 m³ m⁻³ below 40 m. Low water contents at the ADRS were a result of differences in thermal vapor conductivity and liquid hydraulic conductivity of up to five orders of magnitude (Andraski and Jacobson, 2000) indicating that vapor transport is dominant in the unsaturated zone.

Measurements indicate elevated $^3HHO_g$ concentrations throughout the unsaturated zone 100 and 160 m away from the nearest LLRW trench (Fig. 6b and Fig. 6c, respectively). Concentrations of $^3HHO_g$ are reported in units of Bq kg⁻¹ of water in the gas phase. All concentrations of $^3HHO_g$ at the two boreholes are substantially greater than background concentrations ($\leq$3.0 Bq kg⁻¹). Concentrations of $^3HHO_g$ for 2000, 2001, and 2002 at the UZB-3 borehole ranged from 97 to 2704 Bq kg⁻¹ (Fig. 6b). Temporal changes in $^3HHO_g$ concentrations vary with depth. For example, the average coefficient of variation within a depth interval over time was 10% above 40 m and 29% below 40 m. High concentrations of $^3HHO_g$ at 1.5 m coincide with a coarse gravel layer.
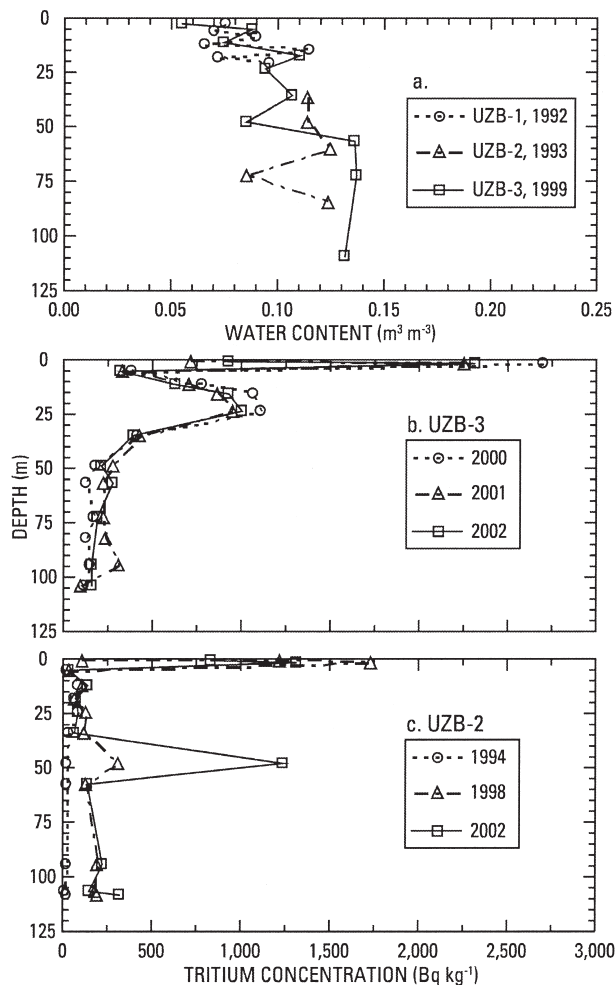
Table 3. Summary of simulations.

	Base case	Source temperature		Source-pressure difference			Source temperature and source-pressure difference			
		35°C	45°C	100 Pa	250 Pa	500 Pa	45°C, 100 Pa	45°C, 250 Pa	45°C, 500 Pa	45°C, 500 Pa, no radioactive decay
Original code	x	x	x	x	x	x	x	x	x	
Modified code†	x	x	x	x	x	x	x	x	x	
Porosity × 0.5	x	x	x	x	x	x	x	x	x	
Porosity × 2.0	x	x	x	x	x	x	x	x	x	
Tortuosity 0.66	x	x	x	x	x	x	x	x	x	
Tortuosity 0.99	x	x	x	x	x	x	x	x	x	
Anisotropy 1 to 10				x	x	x	x	x	x	
Anisotropy 1 to 100				x	x	x	x	x	x	x

† The TOUGH2 code was modified to account for temperature effects on both the Henry's law equilibrium constant for tritium and the isotopic fractionation factor for tritiated water.

Fig. 6. (a) Water content at boreholes UZB-1, UZB-2, and UZB-3. Concentration profiles of tritiated water vapor ($^3HHO_g$) in units of Bq kg^{-1} of water in the gas phase at (b) UZB-3 borehole and (c) UZB-2 borehole for selected years (1994 data from Prudic and Striegl, 1995; 1998 data from Prudic et al., 1999).

Fig. 7. Simulated tritiated water vapor ($^3HHO_g$) concentrations in units of Bq kg^{-1} of water in the gas phase for the reference model simulation at time = 40 yr. Simulated $^3HHO_g$ concentration of 1 Bq kg^{-1} migrated to a maximum horizontal extent (MHE) of 27 m from the vertical face of the source trench and a maximum vertical extent (MVE) of 18 m from the bottom of the source trench.

A large "diffusive-shaped" bulge from 5 to 35 m consists of a cluster of high concentration depth intervals with a maximum $^3HHO_g$ concentration of 1113 Bq kg^{-1} at a depth of 23.8 m. The bulge crosses several layers of gravel and sandy gravel. Concentrations of $^3HHO_g$ for 1994, 1998, and 2002 at the UZB-2 borehole ranged from 16 to 1729 Bq kg^{-1} (Fig. 6c). The average coefficient of variation within a depth interval over time was 37% above 40 m and 85% below 40 m. High concentrations of $^3HHO_g$ at 1.5 and 47.9 m coincide with coarse gravel layers in the unsaturated zone. The tritiated liquid water ($^3HHO_l$) concentration of a groundwater sample from UZB-2 in September 1993 was below detection (<0.36 Bq kg^{-1} of water in the liquid phase). A groundwater sample collected from UZB-3 in March 2000 had a $^3HHO_l$ concentration of 0.45 Bq kg^{-1} of water in the liquid phase.

The UZB-3 and UZB-2 $^3HHO_g$ profiles are similar in the shallow subsurface and differ at depth. Localized surface spills and the LLRW trenches may constitute two different sources of $^3HHO_g$. A near-surface spill may be the cause of concentration peaks at 1.5 m in

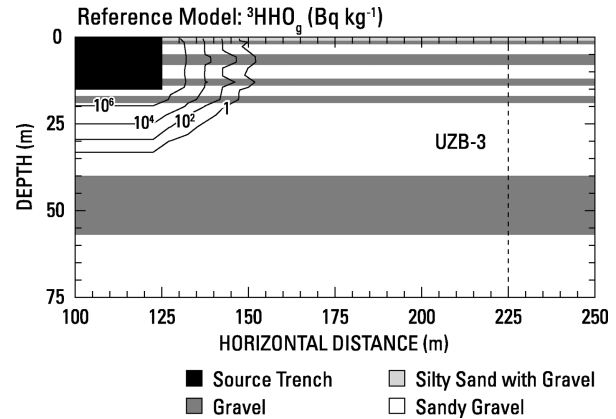both profiles (Andraski et al., 2005). The difference in ^3H distributions at depth for the two profiles indicates two different paths from the LLRW trenches may exist. The close proximity to the 15-m deep trenches may explain the diffusive profile present at UZB-3. A vertical transport path beneath the LLRW facility and then lateral transport through the thick, coarse gravel layer at 50 m may explain the deep UZB-2 profile.

Model Results

Reference Model Simulation Results

The reference model incorporated steady-state conditions previously generated assuming no waste. Initially all ^3H was assigned to the source trench. The extent of simulated transport was evaluated based on the maximum distance that the leading edge of the $^3HHO_g$ plume (defined as 1 Bq kg^{-1} of water in the gas phase) traveled from the horizontal and vertical faces of the source trench. At time = 40 yr, the reference model simulated $^3HHO_g$ migration to a maximum horizontal extent (MHE) of 27 m from the vertical face of the source trench and a maximum vertical extent (MVE) of 18 m from the bottom of the source trench (Fig. 7). The extent and overall shape of the reference model $^3HHO_g$ transport did not match the field data (Fig. 7 and Fig. 6b and 6c, respectively). Compared with the 30-yr model results of Striegl et al. (1996), the reference model increased the horizontal and vertical extents by about 17 and 8 m at time = 30 yr, respectively. Discrepancies between the two model results possibly are because of differences in steady-state water saturations and because a more complex model was used that accounts for temperature effects on the Henry's law equilibrium constant and the isotopic fractionation factor with respect to tritiated water.

Tritium migrated by diffusion in both the liquid and gas phases. Gas-phase diffusion of ^3H dominated due to the low water content of sediments. The average effective-vapor-phase diffusivity (1.9×10^{-5} m^2 s^{-1}) was six orders of magnitude larger than the average effective-liquid-
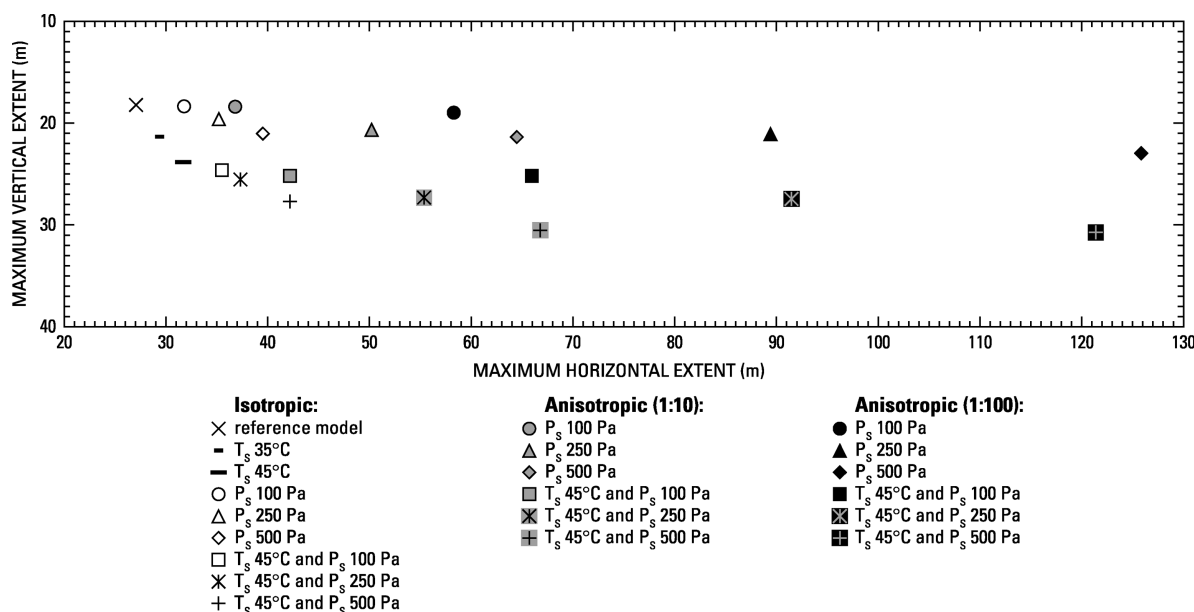
Fig. 8. Summary of simulated tritium (^{3}H) transport as tritiated water vapor (^{3}HHO$_g$) in units of Bq kg^{-1} showing the effects of source temperature (T_S), source-pressure difference above ambient (P_S), and anisotropy on the maximum horizontal extent (MHE) from the vertical face of the source trench and the maximum vertical extent (MVE) from the bottom of the source trench at time = 40 yr. The leading edge of the plume was defined as the concentration of ^{3}HHO$_g$ = 1 Bq kg^{-1} of water in the gas phase.

phase diffusivity (4.0×10^{-11} m^2 s^{-1}). The majority of the ^{3}HHO$_g$ migration occurred in the first 10 yr, during which it traveled approximately 82% of the total MHE and MVE simulated at time = 40 yr. The decline in migration rate after time = 10 yr was due to a decreasing ^{3}H concentration gradient at the leading edge of the plume.

Instantaneous isotopic equilibrium was the primary reason the concentration gradient decreased with time. The amount of ^{3}HHO$_g$ was very small when compared to the nonradioactive liquid water in the soil matrix. Thus, the liquid water in the soil matrix acted as a large sink for ^{3}H, which in turn, substantially reduced the rate and extent of ^{3}HHO$_g$ migration.

Summary of Simulation Results

A summary of the maximum extent of the ^{3}H transport as ^{3}HHO$_g$ for T_S, P_S, and anisotropy simulations is shown in Fig. 8.

Relative to the reference model, both of the isotropic, increased T_S (35 and 45°C) simulations enhanced the transport of ^{3}HHO$_g$ (Fig. 8). However, the T_S values tested were insufficient to enable ^{3}HHO$_g$ to reach either borehole. Henry's law equilibrium constant and isotopic fractionation, with respect to ^{3}H, are temperature dependent. An increased temperature resulted in more ^{3}H partitioning into ^{3}HHO$_g$ and allowed ^{3}HHO$_g$ to migrate further because of the dominance of gas diffusion. The temperature fields generated (not shown) extended less in the horizontal direction than in the vertical direction. The horizontal component was limited by the close proximity of the source trench to the land surface boundary condition (21.8°C) which facilitated rapid heat transfer from the sediments adjacent to the vertical face of the source trench to the surface.

All of the isotropic, increased P_S (100, 250, and 500 Pa) simulations enhanced the migration of ^{3}HHO$_g$ (Fig. 8). However, the P_S values tested were insufficient to enable ^{3}HHO$_g$ to reach either borehole. The pressure effect was greater in the horizontal direction due to the greater permeability of the gravel layers in contact with the vertical edge of the source trench, which in turn increased gas velocities in these layers. The pressure gradients generated for the three isotropic P_S simulations (not shown) were steepest in the horizontal direction away from the source trench due to the close proximity of the land surface boundary condition. Gas velocities in the horizontal direction (averaged over a distance of 15 m) ranged from 2.8×10^{-6} to 1.0×10^{-5} m s^{-1}. In contrast, gas velocities in the vertical direction (averaged over a distance of 15 m) ranged from 1.0×10^{-6} to 5.3×10^{-6} m s^{-1}.

All of the isotropic, increased T_S-and-P_S combination simulations enhanced the migration of ^{3}HHO$_g$ (Fig. 8). However, the T_S-and-P_S combinations tested were insufficient to enable ^{3}HHO$_g$ to reach either borehole. The combined effects of T_S and P_S were additive, yielding a ^{3}HHOg field that extended further in the horizontal direction than in the vertical direction. The T_S component affected both the horizontal and vertical transport of ^{3}HHO$_g$, whereas the P_S component primarily affected the horizontal transport of ^{3}HHO$_g$.

To further evaluate the code modification (Eq. [11] and Eq. [12]), all of the aforementioned simulations were run without the code modification. Results showed the code modifications substantially affected all isotropic simulations that incorporated an increased T_S. For example, average MHE and MVE increases of 12 and 24%, respectively, were realized in modified code simulations with an increased T_S. In contrast, in simulations

without an increased T_S, the modified code yielded average MHE and MVE increases of 1 and 1%, respectively.

The porosity simulations yielded little change in the MHE and MVE of the $^3HHO_g$ field generated (not shown). One effect of changing the porosity was in the temperature field, which resulted in a small concomitant change in the $^3HHO_g$ field. Changing the porosity did not affect the ratio of gas and liquid in the pores; however, the relative soil solid to pore volume did change which resulted in an altered temperature field. Another effect of changing the porosity was the change in the liquid water available for ^3H exchange. An increase in water content resulted in more ^3H partitioning into the liquid water and a diminished rate of $^3HHO_g$ transport. The porosity factor of 0.5 and 2 simulations generated $^3HHO_g$ fields that were within 6 and 4 m of their unadjusted counterparts, respectively.

All of the tortuosity simulations based on the relative permeability model slightly increased the MHE and MVE of $^3HHO_g$ migration when compared to the Millington (1959) tortuosity model (not shown). This occurred because the relative permeability model used a tortuosity factor of 0.66 or 0.99, whereas the Millington (1959) model resulted tortuosity factors that ranged from 0.57 to 0.69 with an average tortuosity factor of 0.61 (upper 30 m of the unsaturated zone). However, even with a tortuosity factor of 0.99 the enhancement was small. The simulations using a tortuosity factor of 0.66 and 0.99 resulted in increased maximum extents of the $^3HHO_g$ fields up to 2 and 6 m of their unadjusted counterparts, respectively. The relatively small effect of tortuosity appears to be due to the dominant effect of instantaneous isotopic equilibrium on the extent of ^3H migration.

The anisotropic simulations increased the MHE and MVE of the $^3HHO_g$ migration (Fig. 8). The anisotropic MHE increased by as much as 86 m, whereas the largest MVE increase was 3 m when compared to isotropic counterparts at time = 40 yr. Changing the intrinsic permeabilities affected the simulated pressure fields and enhanced $^3HHO_g$ transport in the horizontal direction, but did not affect the simulated temperature fields. Changes in T_S did influence the anisotropic simulations with increased temperature fields leading to a preferential migration of $^3HHO_g$ in the vertical vs. horizontal direction. Two of the 1:100 anisotropic simulations [P_S 500 Pa; T_S 45°C and P_S 500 Pa combination (Fig. 8)] allowed the $^3HHO_g$ to migrate a horizontal distance equivalent to that necessary to reach the UZB-3 borehole. Although the simulated $^3HHO_g$ plumes extended past UZB-3, the simulated concentrations were a fraction of the measured concentrations shown in Fig. 6b.

An additional simulation was completed to evaluate the effect of radioactive decay on the maximum extent of the $^3HHO_g$ transport. The simulation was anisotropic (1:100), T_S 45°C, P_S 500 Pa and ^3H was not allowed to decay. The $^3HHO_g$ field generated at time = 40 yr (not shown) had a MHE of 123 m and a MVE of 31 m; these values were only slightly greater (<2 m) than those for the same simulation that allowed ^3H to decay. Thus,

radioactive decay was not a limiting factor in the transport of $^3HHO_g$.

Representative "Shape" of Simulated $^3HHO_g$ Fields

Results of selected simulations shown in Fig. 9 illustrate variations in the "shape" of the simulated $^3HHO_g$ fields. The shape of the $^3HHO_g$ field for the T_S 45°C simulation (Fig. 9a) reflects diffusive transport enhanced by T_S. Relative to the reference model simulation (Fig. 7), the MHE and MVE of the $^3HHO_g$ field increased 5 and 6 m at time = 40 yr, respectively. The shape of the $^3HHO_g$ field for the P_S 500 Pa simulation (Fig. 9b) was similar to that for the T_S 45°C simulation (Fig. 9a), but the MVE was smaller. Relative to the reference model, the MHE and MVE of the $^3HHO_g$ field increased 12 and 3 m at time = 40 yr, respectively. The combined effects of T_S and P_S for the isotropic T_S 45°C and P_S 500 Pa simulation were additive (Fig. 9c). Relative to the reference model, the MHE and MVE of the $^3HHO_g$ field increased 15 and 9 m at time = 40 yr, respectively. The simulated $^3HHO_g$ fields shown in Fig. 9a, Fig. 9b, and Fig. 9c not only failed to transport $^3HHO_g$ to the UZB-3 and UZB-2 boreholes, but did not resemble the measured profile at either UZB-3 or UZB-2 (Fig. 6b and Fig. 6c, respectively).

The $^3HHO_g$ field generated for the anisotropic (1:100) T_S 45°C and P_S 500 Pa simulation (Fig. 9d) resembled the upper portion of the UZB-3 $^3HHO_g$ profile (Fig. 6b). Relative to the reference model, the MHE and MVE of the $^3HHO_g$ field increased 94 and 13 m at time = 40 yr, respectively. Increasing the horizontal intrinsic permeability resulted in greater $^3HHO_g$ transport in the horizontal direction. The anisotropy allowed the pressure imposed at the source trench to escape laterally instead of creating an increased vertical pressure gradient beneath the source trench. This preferential flow enabled $^3HHO_g$ to migrate further away from the source trench. All of the anisotropic simulations generated $^3HHO_g$ fields that resembled the near surface profiles measured at the UZB-3 $^3HHO_g$ borehole (Fig. 6b). The simulations showed increased $^3HHO_g$ concentrations between land surface and a depth of 46 m, with a peak concentration at approximately 18 m. In contrast with the field data (Fig. 6b and Fig. 6c); however, none of the simulated $^3HHO_g$ fields showed vertical migration of $^3HHO_g$ below 46 m.

CONCLUSIONS

Field data for water content and concentrations of tritiated water vapor ($^3HHO_g$) in the 100-m deep unsaturated zone indicate that ^3H movement primarily occurs in the gas phase with preferential transport through coarse-textured sediment layers. The UZB-3 and UZB-2 borehole profiles have the highest concentrations at a 1.5-m depth that correspond with a dry, coarse-gravel layer. At depth, the shapes of the two profiles differ considerably. The high $^3HHO_g$ concentrations at UZB-3 (100 m from the nearest LLRW trench) are seen as a bulge between 5 and 35 m. The bulge crosses several
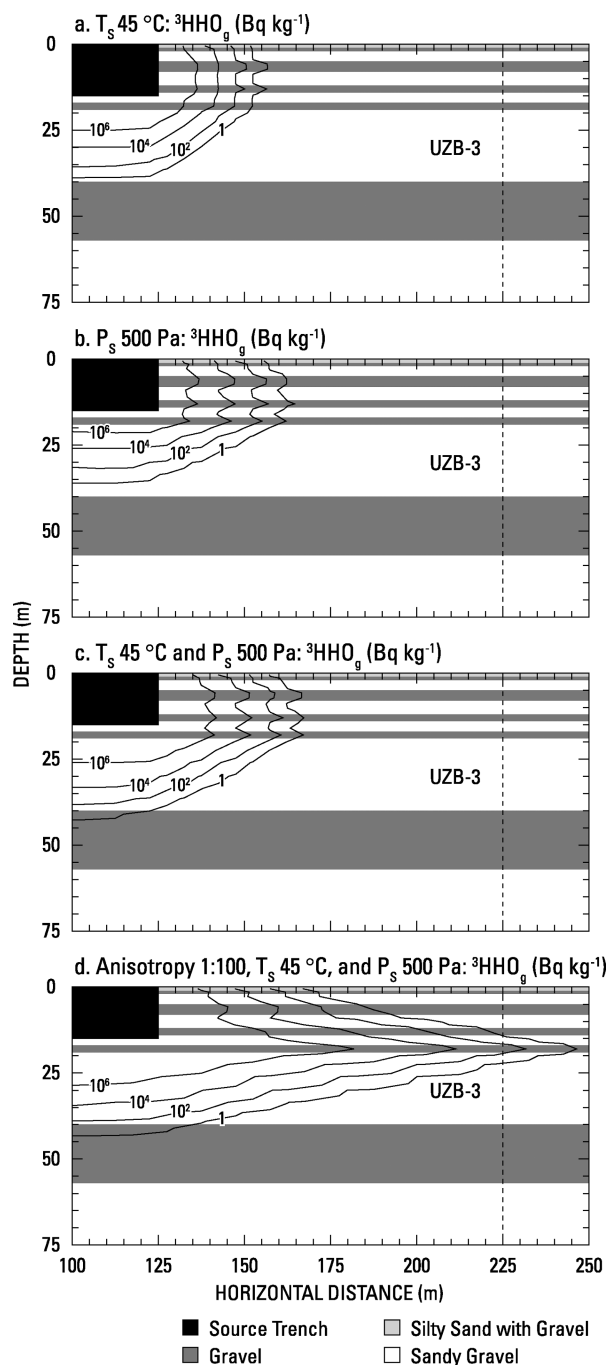
Fig. 9. Simulated tritiated water vapor ($^3HHO_g$) concentrations in units of Bq kg^{-1} of water in the gas phase at time = 40 yr for (a) source temperature (T_S) 45°C simulation [maximum horizontal extent (MHE) = 32 m and a maximum vertical extent (MVE) = 24 m], (b) source-pressure difference above ambient (P_S) 500 Pa simulation (MHE = 40 m and MVE = 21 m), (c) T_S 45°C and P_S 500 Pa simulation (MHE = 42 m and MVE = 28 m), and (d) anisotropic (1:100), T_S 45°C, and P_S 500 Pa simulation (MHE = 121 m and MVE = 31 m). The MHE and MVE values are based on a simulated $^3HHO_g$ concentration of 1 Bq kg^{-1}.

layers of sandy gravel and gravel. In contrast, the high $^3HHO_g$ concentration at UZB-2 (160 m from the nearest LLRW trench) is present at a single sampling depth, 47.9 m, which is within an individual gravel layer.

All isotropic simulations were insufficient to transport

$^3HHO_g$ to distances that would reach one or both of the boreholes. The inability to transport $^3HHO_g$ resulted from a decreasing concentration gradient because of instantaneous isotopic equilibrium between the liquid and vapor phases. In the reference model simulation, the dominant transport mechanism was diffusion in the gas phase. Code modification incorporating the temperature dependence of both the Henry's law equilibrium constant and fractionation with respect to tritiated water was important in realizing the effects of increased T_S. All of the elevated T_S simulations enhanced the migration of $^3HHO_g$ because the increased temperature field allowed more ^3H to partition into $^3HHO_g$. All of the increased source-pressure-difference (P_S) simulations enhanced the migration of $^3HHO_g$. The enhancement was greater in the horizontal direction because of the contact between the source trench and the near surface gravel layers. The combined effects of T_S and P_S were additive, yielding a $^3HHO_g$ field that extended further in the horizontal direction than in the vertical direction. The temperature component affected both the horizontal and vertical transport of $^3HHO_g$, whereas the pressure component primarily affected the horizontal transport of $^3HHO_g$. Changes in porosity and tortuosity had little affect on transport of $^3HHO_g$.

The anisotropic simulations showed the greatest enhancement of $^3HHO_g$ transport. The horizontal component increased substantially (5–86 m) whereas the vertical component increased only slightly (0–3 m) when compared to the equivalent isotropic simulations. All of the anisotropic simulations with a P_S component generated $^3HHO_g$ fields that resembled the upper portion (5–50 m) of the measured UZB-3 $^3HHO_g$ profile. Simulation results indicated that a high degree of anisotropy (1:100) in conjunction with a P_S component of 500 Pa was necessary for $^3HHO_g$ to reach the UZB-3 borehole.

None of the simulations in this study were able to reproduce observed $^3HHO_g$ profiles. Simulations showed that radioactive decay did not limit the migration of $^3HHO_g$. However, isotopic equilibrium in which liquid water in the soil matrix acted as a large sink for the $^3HHO_g$ appeared to be a major limiting factor in the migration of $^3HHO_g$. The failure to match simulated ^3H profiles to measured profiles is likely due to insufficiencies in the conceptual model. A process that has not yet been accounted for may be driving ^3H transport in the deep unsaturated zone. Possible mechanisms driving ^3H transport that need to be explored include coupled transport of ^3H and volatile organic compounds and the effects of barometric pumping. Additional fieldwork is also needed to better quantify permeabilities and anisotropy.

REFERENCES

Andraski, B.J. 1996. Properties and variability of soil and trench fill at an arid waste-burial site. Soil Sci. Soc. Am. J. 60:54–66.

Andraski, B.J. 1997. Soil-water movement under natural-site and waste-site conditions: A multiple-year field study in the Mojave Desert, Nevada. Water Resour. Res. 33:1901–1916.

Andraski, B.J., and E.A. Jacobson. 2000. Testing a full-range soil-water retention function in modeling water potential and temperature. Water Resour. Res. 36:3081–3089.

Andraski, B.J., D.A. Stonestrom, R.L. Michel, K.J. Halford, and J.C. Radyk. 2005. Plant-based plume-scale mapping of tritium contamination in desert soils. Available at www.vadosezonejournal.org. Vadose Zone J. 4:819–827.

Atkins, P.W. 1978. Physical chemistry. W.H. Freeman and Co., San Francisco, CA.

Carslaw, H.S., and J.C. Jaeger. 1959 Conduction of heat in solids. 2nd ed. Oxford Univ. Press, New York.

Corey, A.T. 1954. The interrelation between gas and oil relative permeabilities. Producers Monthly, November, 38–41

Crawford, J.F., and P.G. Smith. 1985. Landfill technology. Butterworths, London.

Cussler, E.L. 1997. Diffusion: Mass transfer in fluid systems. Cambridge Univ. Press, New York.

Evans, E. 1974. Tritium and its compounds. John Wiley & Sons, New York, N.Y.

Fentiman, A.W., J.E. Meredith, and R.J. Veley. 1993. What is low-level radioactive waste? [Online]. Available at www.ag.ohio-state.edu/~rer/rerhtml/rer_10.html (accessed 5 November 2002; verified 12 Aug. 2005). Ohio State Univ. Extension, Columbus.

Fischer, J.M. 1992. Sediment properties and water movement through shallow unsaturated alluvium at an arid site for disposal of low-level radioactive waste near Beatty, Nye County, Nevada. WRIR 92–4032. U.S. Geol. Surv., Carson City, NV.

Ferronsky, V.I., and V.A. Polyakov. 1982. Environmental isotopes in the hydrosphere. John Wiley & Sons, New York.

Freeze, R., and J. Cherry. 1979. Groundwater. Prentice Hall, Edgewood Cliffs, NJ.

Gee, G.W., and D. Or. 2002. Particle-size analysis. p. 255–289. In J.H. Dane and G.C. Topp et al. (ed.) Methods of soil analysis. Part 4. Physical methods. SSSA, Madison, WI.

Healy, R.W., R.G. Striegl, R.L. Michel, D.E. Prudic, and B.J. Andraski. 1999. Tritium in water vapor in the shallow unsaturated zone at the Amargosa Desert Research site. In D.W. Morganwalp and H.T. Buxton (ed.) U.S. Geol. Surv. Toxic Substances Hydrology Program–Proc. of the Technical Meet., Charleston, SC. 8–12 Mar. 1999. Vol. 3. Subsurface contamination from point sources. WRIR 99–4018-C:485–490. U.S. Geol. Surv., West Trenton, NJ.

Knight, J.H. 1996. An improved approximation for spherical diffusion of tritium in relatively dry soil. Water Resour. Res. 32:349–354.

Logan, S.R. 1996. Fundamentals of chemical kinetics. Longman Group Limited, Essex, England.

Millington, R.J. 1959. Gas diffusion in porous media. Science (Washington, DC) 130:100–102.

Mills, R. 1973. Self-diffusion in normal and heavy water in the range 1–45°. J. Phys. Chem. 77:685–688.

Mualem, Y.A. 1976. A new model for predicting the hydraulic conductivity of unsaturated porous media. Water Resour. Res. 12:513–522.

Pruess, K.A., C. Oldenburg, and G. Moridis. 1999. TOUGH2 user's guide. Version 2.0. LBNL-43134. Lawrence Berkeley Natl. Lab., Berkeley, CA.

Prudic, D.E., D.A. Stonestrom, and R.G. Striegl. 1997. Tritium, deuterium, and oxygen-18 in water collected from unsaturated sediments near a low-level radioactive-waste burial site south of Beatty, Nevada. WRIR 97–4062. U.S. Geol. Surv., Carson City, NV.

Prudic, D.E., and R.G. Striegl. 1995. Tritium and radioactive carbon (^{14}C) analyses of gas collected from unsaturated sediments next to a low-level radioactive-waste burial site south of Beatty, Nevada, April 1994 and July 1995: OFR 95–741. U.S. Geol. Surv., Carson City, NV.

Prudic, D.E., R.G. Striegl, R.W. Healy, R.L. Michel, and H. Haas. 1999. Tritium and ^{14}C concentrations in unsaturated-zone gases at test hole UZB-2, Amargosa Desert Research Site, 1994–98. In D.W. Morganwalp, and H.T. Buxton (ed.) U.S. Geol. Surv. Toxic Substances Hydrology Program. Proc. of the Technical Meet., Charleston, SC. 8–12 Mar. 1999. Vol. 3 of 3–Subsurface contamination from point sources. WRIR 99–4018-C:475–484. U.S. Geol. Surv., West Trenton, NJ.

Scanlon, B.R., K. Keese, R.C. Reedy, J. Simunek, and B.J. Andraski. 2003. Variations in flow and transport in thick desert vadose zones in response to paleoclimatic forcing (0–90 kyr)–Field measurements, modeling, and uncertainties. Water Resour. Res. 39:3-1–3-17.

Smiles, D.E., W.R. Gardner, and R.K. Schulz. 1995. Diffusion of tritium in arid disposal sites. Water Resour. Res. 31:1483–1488.

Striegl, R.G. 1988. Distribution of gases in the unsaturated zone at a low-level radioactive-waste disposal site near Sheffield, Illinois. WRIR 88–4025. U.S. Geol. Surv., Urbana, IL.

Striegl, R.G., D.E. Prudic, J.S. Duval, R.W. Healy, E.R. Landa, D.W. Pollock, D.C. Thorstenson, and E.P. Weeks. 1996. Factors affecting tritium and ^{14}carbon distributions in the unsaturated zone near the low-level radioactive-waste burial site south of Beatty, Nevada, April 1994 and July 1995. OFR 96–110. U.S. Geol. Surv., Denver, CO.

Thatcher, L.L., V.J. Janzer, and K.W. Edwards. 1977. Methods for determination of radioactive substances in water and fluvial sediments. USGS Techniques of Water Resour. Invest. Book 5, Chap. A5. U.S. Gov. Print Office, Washington, DC.

U.S. Nuclear Regulatory Commission. Office of Inspection and Enforcement, Region V. 1976. IE Inspection Rep. 76–02. U.S. Nuclear Regulatory Commission Region V, Walnut Creek, CA.

van Genuchten, M.Th. 1980. A closed-form equation for predicting the hydraulic conductivity of unsaturated soils. Soil Sci. Soc. Am. J. 44:892–898.

Vargaftik, N.B. 1975. Tables on the thermophysical properties of liquids and gases. 2nd ed. John Wiley & Sons, New York.

Walvoord, M.A., D.A. Stonestrom, B.J. Andraski, and R.G. Striegl. 2004. Constraining the inferred paleohydrologic evolution of a deep unsaturated zone in the Amargosa Desert. Available at www.vadosezonejournal.org. Vadose Zone J. 3:502–512.